Observations of Misovortices within a Long-lake-axis-parallel Lake-effect Snow Band during the OWLeS Project

JAKE MULHOLLAND*, JEFFREY FRAME, AND STEPHEN NESBITT

Department of Atmospheric Sciences, University of Illinois at Urbana-Champaign, Urbana, IL

SCOTT STEIGER

State University of New York at Oswego, Oswego, NY

KAREN KOSIBA AND JOSHUA WURMAN

Center for Severe Weather Research, Boulder, CO

1. Introduction and motivation

On 7 January 2014, an intense long-lake-axis-parallel (LLAP) lake-effect snow band developed over Lake Ontario during Intensive Observation Period 7 (IOP-7) of the Ontario Winter Lake-effect Systems (OWLeS) Project (Kristovich et al. 2017). This band formed in response to Arctic air, characterized by 850 mb temperatures on the order of –25°C, passing over the relatively warm 3°C waters of Lake Ontario. The resultant lake surface to 850 mb temperature difference of 28°C was more than twice the requisite 13°C required for the formation of intense lake-effect convection (Phillips 1972). Persistent northwesterly to westerly cyclonic boundary layer flow continued to advect cold air over Lake Ontario, ultimately resulting in a long-duration lake-effect event, with snowfall amounts in some locations exceeding 150 cm.

The lake-effect band developed around 0200 UTC 7 January and persisted well into 8 January; owing to crew fatigue and extremely cold temperatures, however, OWLeS ground teams (including multiple ground-based mobile Doppler radars) only collected data from 0200–2230 UTC 7 January. Soon after its formation, the lake-effect band exhibited a prominent connection with an upstream LLAP band that had formed over Georgian Bay (Fig. 1). This connection is evidenced via the horizontal extrapolation of upstream radar echoes, indicating the advection of a lake-modified boundary layer toward the downstream lake.

Since the first high-resolution, mobile Doppler radar observations of LLAP bands were attempted during the winter of 2010-11, numerous instances of misoscale vortices have been observed within these bands (e.g., Steiger et al. 2013; Conrad et al. 2015), often organized into strings. Previous analysis of single-Doppler data has postulated that such strings of vortices originate owing to the release of horizontal shearing instability (HSI) along horizontal wind shifts and cyclonic shear zones within the bands, often coincident with the ascending branch of the transverse circulation (Steiger et al. 2013). Since only single-Doppler data were available to Steiger et al. (2013), however, no definitive conclusion could be reached as to the origin of these strings of misovortices since the construction of three-dimensional wind syntheses was not possible.

It is the aim of the present study to document an additional case of a string of misovortices within an LLAP lake-effect band, and, through the analysis of three-dimensional dual-Doppler wind syntheses and the use of a high-resolution Weather Research and Forecasting (WRF) model simulation, demonstrate that two instability criteria for the release of HSI are satisfied along the shear zone where the vortices are found and that these vortices are maintained across the lake via vortex stretching.

Our data and analysis methods are outlined in section 2, and section 3 contains the dual-Doppler analysis. The analysis of the WRF simulation is in section 4, and a summary of our conclusions is found in section 5.

2. Data and methodology

a. Dual-Doppler wind syntheses

Data from two Doppler radars (DOW6 and DOW8; Wurman et al. 1997) were edited for quality control with Solo3 software (Bell et al. 2013) such that regions of data characterized by beam blockage from ground targets, ground clutter, sea spray, or a low signal-to-noise ratio were removed (see Mulholland et al. 2017 for a full description of this process). The data were then mapped to a Cartesian grid using a two-pass Barnes anal-

**Corresponding author address*: Jake Mulholland, Department of Atmospheric Sciences, University of Illinois at Urbana-Champaign, 1201 W. Green St., Urbana, IL, 61801; *e-mail*: jmulhol2@illinois.edu

ysis (Barnes 1964). The Cartesian grid dimensions are 40 × 40 × 2.5 km, with a horizontal and vertical grid spacing of 250 m. Smoothing parameters of $\kappa_H = 0.747$ km^2 in the horizontal and $\kappa_Z = 0.400$ km^2 in the vertical were used. The difference in the smoothing parameters was necessitated because all elevation scans between 1–2° from DOW8 were missing owing to a mechanical failure. The extrapolation of data into voids was not permitted during the objective analysis, which resulted in qualitatively better kinematic fields in the three-dimensional wind syntheses. The specifications of the dual-Doppler analysis are consistent with guidelines provided by Pauley and Wu (1990) and Majcen et al. (2008). The wind syntheses were constructed via an upward integration of the anelastic continuity equation from the bottom of the dual-Doppler domain following the method outlined in the appendix of Kosiba et al. (2013). The radar deployment map and dual-Doppler lobe are displayed in Fig. 2.

b. *WRF model configuration*

The WRF model (version 3.7.1; Skamarock et al. 2008) was used to conduct a high-resolution simulation of this case. The innermost grid has a horizontal resolution of 333 m (258 × 147 km) and is nested within 1 km (636 × 438 km) and 3 km (1335 × 882 km) grids (Fig. 3). The outermost domain was initialized from the 0000 UTC 7 January 2014 Rapid Refresh (RAP) model. The 333-m grid spacing on the innermost grid is comparable to the 250 m horizontal resolution of the dual-Doppler grid, allowing for a nearly one-to-one comparison of vortex characteristics including strength, speed, and depth.

The model simulation utilized 60 vertical levels; the top of the model domain was at 50 mb. No damping layer was implemented near the model top owing to the relatively shallow depth of the band (< 5 km above ground level [AGL]) and short duration of the model integration (12 h). A vertically-stretched grid was utilized, with the lowest model level located at 75 m AGL. The vertical grid spacing near the surface is 75 m and decreases to approximately 750 m near the model top. The model was run on the Arakawa C-grid with Runge-Kutta 2nd and 3rd order time integration schemes. The Thompson microphysical scheme (Thompson et al. 2008) was employed along with the Rapid Radiative Transfer Model GCM (RRTMG) longwave and shortwave radiation schemes (Iacono et al. 2008), the Rapid Update Cycle (RUC) land surface model (LSM; Smirnova et al. 2016), the revised Pennsylvania State University (PSU)/National Center for Atmospheric Research (NCAR) Mesoscale Model (MM5) Monin-Obukov surface-layer scheme (Jiménez

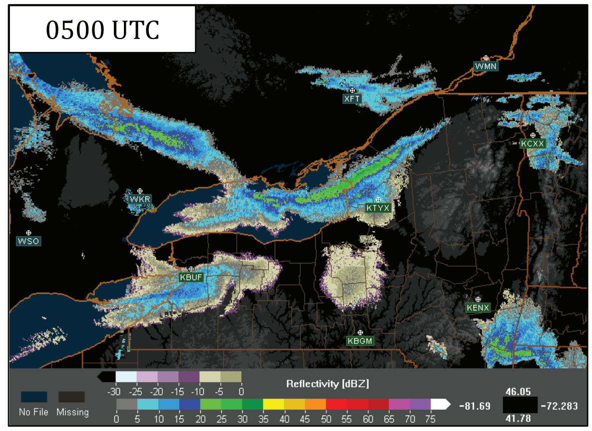

FIG. 1. Multi-radar multi-sensor (MRMS) analysis over the eastern Great Lakes region at 0500 UTC 7 January 2014.

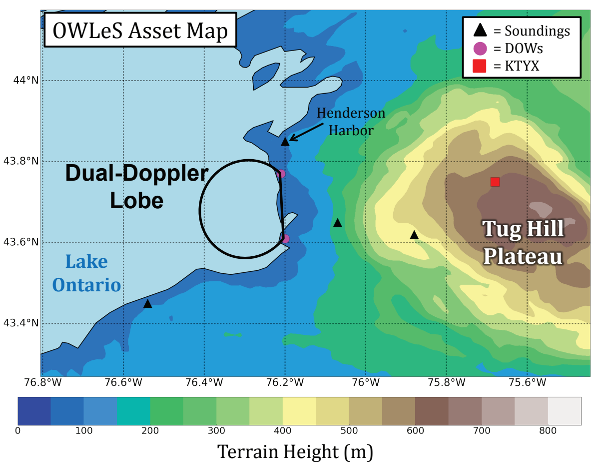

FIG. 2. Map illustrating the locations of mobile radars (pink circles), mobile sounding units (black triangles), and the KTYX WSR-88D radar (red square). The dual-Doppler lobe is indicated in black and terrain height (m) is shaded.

et al. 2012), and the new Shin-Hong (S-H; Shin and Hong 2015) boundary layer parametrization. No cumulus parametrization was implemented at any grid scale.

3. Dual-Doppler analysis

Six distinct cyclonic misovortices were tracked for a period of greater than 30 minutes, although only a shorter 20-minute analysis period is presented here (Fig. 4). Neither anticyclonic vortices nor counter-rotating vortex

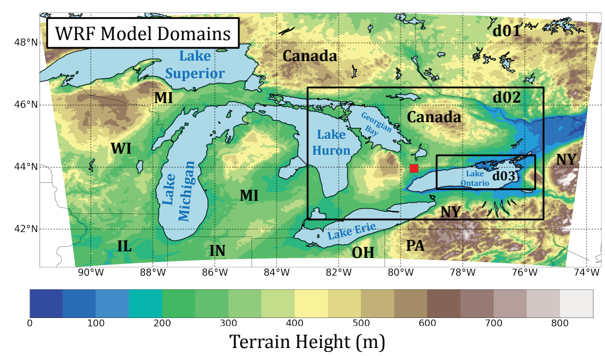

FIG. 3. Map illustrating the three nested WRF domains, with horizontal resolutions of 3 km, 1 km, and 333 m. Terrain height (m) is shaded.

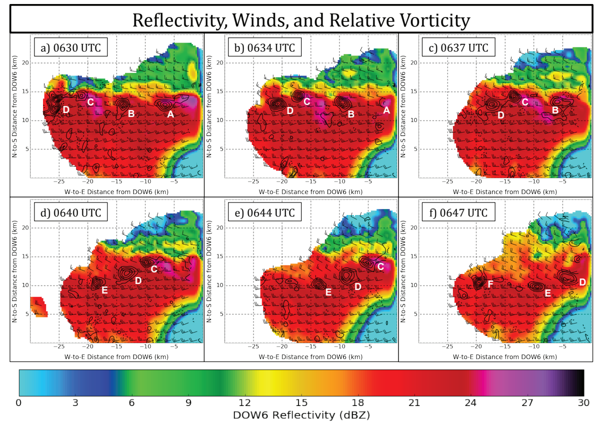

FIG. 4. Dual-Doppler wind syntheses at 500 m AGL with horizontal winds (full barb = 10 m s^{-1}), DOW6 composite reflectivity (dBZ; shaded), and vertical vorticity (contoured every 0.5 x 10^{-2} s^{-1}) at: a) 0630, b) 0634, c) 0637, d) 0640, e) 0644, and f) 0647 UTC 7 January 2014. Each vortex is labeled with a capital letter.

couplets were observed during this event. During this time period, the vortices did not merge or interact with each other in any way. The vortices tracked along a cyclonic horizontal shear zone near the northern edge of the snow band, evidenced by faster westerly winds, on the order of 25 m s^{-1}, south of the shear zone, and slower westerly winds, on the order of 15 m s^{-1}, north of the shear zone. The vortices moved east-southeastward at an average speed of 19 m s^{-1}, nearly matching the mean zonal wind in the 0-2 km AGL vortex-bearing layer. By 0644 UTC, the vortices moved toward the center of the band (Fig. 4e). Peak vertical vorticity values within the vortices ranged from $1-3\times10^{-2}$ s^{-1}, which is consistent with those documented in previous studies of misovortices (e.g., Mueller and Carbone 1987; Lee and Wilhelmson 1997; Arnott et al. 2006; Buban et al. 2007; Marquis et al. 2007; Campbell et al. 2014). Curiously, the string of vortices dissipated when the connection between the Georgian Bay and Lake Ontario bands (Fig. 1) ceased as boundary layer winds backed from northwesterly to westerly over the upstream lakes.

A vertical cross section through one of the vortices (Vortex A) at 0630 UTC reveals that the primary band updraft, associated with the secondary in-up-and-out circulation within the band, was also along the northern edge of the band, just north of the position of the vortices (Fig. 5). Significant overlap between cyclonic vertical vorticity and upward vertical velocity suggests that stretching is likely important to vortex maintenance over the lake. Indeed, a plot of the stretching term in the vertical vorticity equation, $\zeta\frac{\partial w}{\partial z}$, where ζ is the relative vertical vorticity and w is the vertical velocity, reveals that stretching was active in most of the vortices at 500 m AGL (Fig. 6).

Rayleigh's Instability Criterion (hereafter RIC), scaled for mesoscale processes, states that $\frac{\partial^2\bar{u}}{\partial y^2}$ must change sign somewhere in the flow for HSI to exist, where $\bar{u}$ is the horizontal wind component parallel to the shear zone (here taken to be the zonal wind component) averaged along the shear zone (Markowski and Richardson 2010, p 63-64). A plot of this quantity in the north-south direction at 0630 UTC reveals that a sign change exists 11–12 km north of the location of DOW6 (Fig. 7), which is also where the vortices are present at this time (Fig. 4a). Although this quantity approaches zero at other locations, these are generally located near the edges of the dual-Doppler domain, where calculating derivatives is more prone to errors.

A more stringent criterion, Fjørtoft's Instability Criterion (hereafter FIC), states that $\frac{\partial^2\bar{u}}{\partial y^2}(\bar{u}-\bar{u}_I)<0$ for HSI, where $\bar{u}_I$ is the mean wind component parallel to the shear zone at the inflection point (i.e., where $\frac{\partial^2\bar{u}}{\partial y^2}$ vanishes in Fig. 7). This criterion is satisfied in a broad zone encompassing the shear zone and vortices (Figs. 4a and 8). Although both RIC and FIC are necessary but not sufficient conditions for the release of HSI, and that dual-Doppler observations of the genesis of these vortices do not exist, the satisfaction of both RIC and FIC combined with the lack of any cyclonic-anticyclonic vortex couplets strongly suggests that HSI, and not tilting of ambient horizontal vorticity owing to the environmental vertical wind shear or frictional processes, is the dominant formation mechanism of these vortices.

Both RIC and FIC are consistently satisfied at the location of the shear zone and vortices throughout this analysis period. For a more detailed analysis of these other times, please see Mulholland et al. (2017).

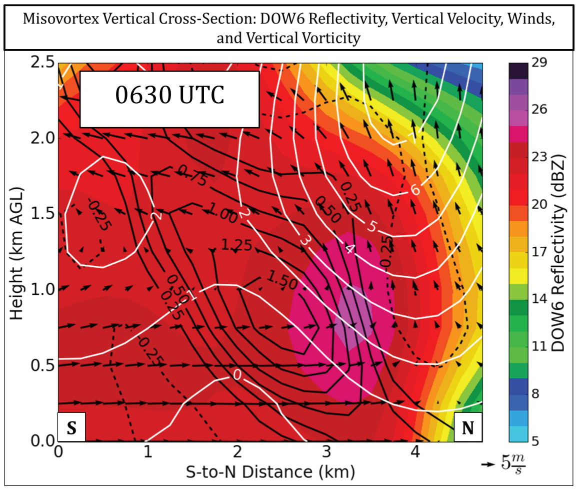

FIG. 5. South-to-north vertical cross section through Vortex A in Fig. 4a at 0630 UTC with DOW6 reflectivity (dBZ; shaded), vertical velocity (white contours every 1 m s^{-1}), vertical vorticity (black contours every 0.25 × 10^{-2} s^{-1}), and wind vectors (v and w components only; m s^{-1}).

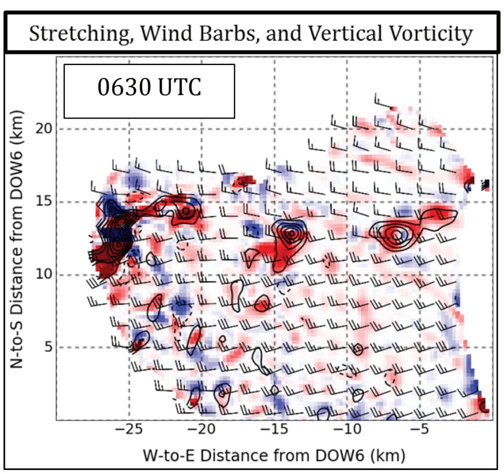

FIG. 6. Stretching term in the vertical vorticity equation ($\zeta\frac{\partial w}{\partial z} \times 10^{-4}$ s^{-2}; shaded), 500 m winds (full barb = 10 m s^{-1}), and vertical vorticity (contoured every 0.5 × 10^{-2} s^{-1}) at 0630 UTC.

4. WRF simulation analysis

The high-resolution WRF simulation replicates the synoptic and thermodynamic environment (not shown) and produces a realistic LLAP snow band over Lake Ontario which contains a string of misovortices along its northern edge (Fig. 9). Owing to spin-up time associated with a cold start of the model at 0000 UTC 7 January, the simulated snow band evolves about 1–2 hours later than what was observed. As in the observations, all of the misovortices are cyclonic, strongly suggesting that tilting is not a likely generation mechanism of the simulated vor-

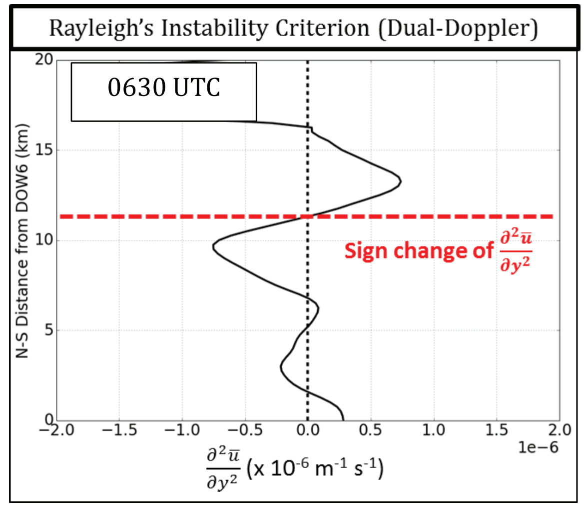

FIG. 7. RIC ($\frac{\partial^2 \bar{u}}{\partial y^2} \times 10^{-6}$ m^{-1} s^{-1}) vs. north-south distance (km) from DOW6 at 500 m AGL at 0630 UTC. The red dashed line indicates where RIC is satisfied.

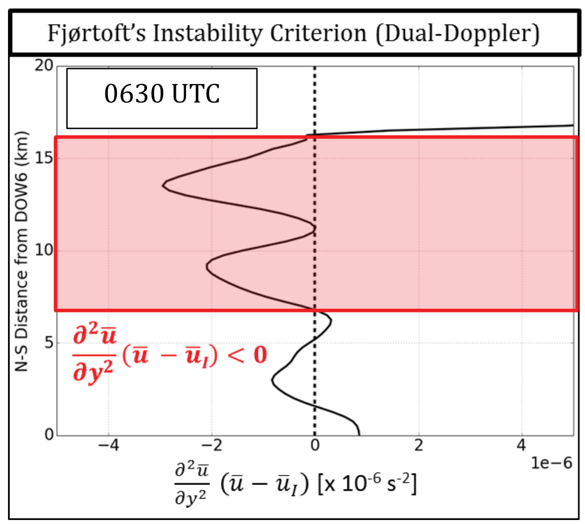

FIG. 8. FIC ($\frac{\partial^2 \bar{u}}{\partial y^2}(\bar{u} - \bar{u}_I) \times 10^{-6}$ s^{-2}) vs. north-south distance (km) from DOW6 at 500 m AGL at 0630 UTC. The red shading indicates where FIC is satisfied.

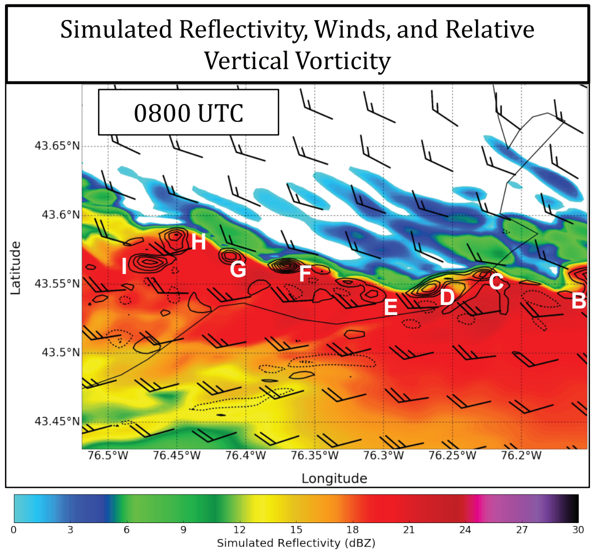

FIG. 9. Simulated composite reflectivity (dBZ, shaded) with horizontal winds (full barb = 10 m s^{-1}), and relative vertical vorticity (contoured every 0.5×10^{-2} s^{-1}) at 500 m AGL at 0800 UTC 7 January 2014. Each vortex is labeled with a capital letter.

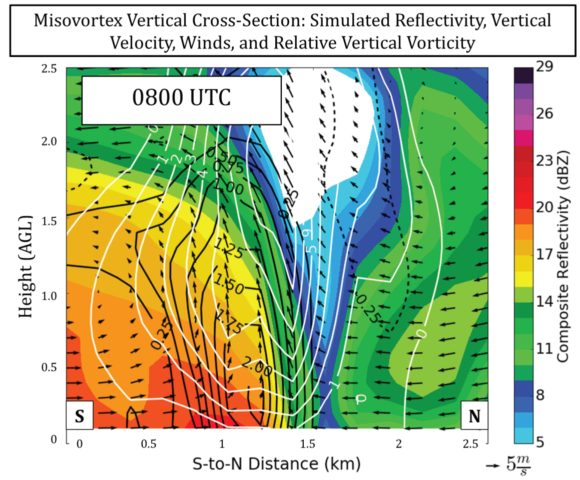

FIG. 10. South-to-north vertical cross-section through simulated Vortex G at 0800 UTC, with composite reflectivity (dBZ; shaded), vertical velocity (white contours every 1 m s^{-1}), vertical vorticity (black contours every 0.25×10^{-2} s^{-1}), and wind vectors (v and w components only; m s^{-1}).

tices either. A vertical cross section through one of the simulated vortices (Vortex G; Fig. 10) at 0800 UTC further reveals that the vortices are just south of the ascending branch of the secondary circulation as in the observations and that there is again a significant overlap in the vertical velocity and vorticity fields. A closer inspection of the stretching term in the vertical vorticity equation (Fig. 11) reveals that most vortices are associated with nonzero values of stretching over the lake, as in the dual-Doppler analysis. WRF output is also available over land (the inland-directed radar beams were blocked by heavy tree cover along the shoreline), and depicts the simulated vortices weakening rapidly as they move inland, likely owing to increased surface roughness. This weakening also lends support to the hypothesis that stretching is an important vortex maintenance mechanism over the lake since the values of stretching within the vortices also diminish greatly with inland extent, commensurate with the movement of the vortices from a less statically-stable environment over the water to a more statically-stable environment over land.

In the WRF simulation, RIC is satisfied near latitude 43.55°N (Fig. 12), which is also the location of the vortices and shear zone (Fig. 9). FIC is also satisfied in a broader zone encompassing this latitude (Fig. 13), lending further support to the conclusion reached above that HSI, not vortex tilting, is the likely generation mechanism of the string of misovortices observed in this case. Analyses of other times in the WRF simulation has been completed by Mulholland et al. (2017) and reveals that both RIC and FIC are satisfied at the location of the vortices and shear zone at these times.

5. Conclusions

Dual-Doppler observations and a high-resolution WRF simulation of a long-lived intense LLAP lake-effect snow band on 7 January 2014 that contained a string of misovortices are analyzed herein. The simulation realistically reproduced the synoptic and mesoscale environment in the vicinity of Lake Ontario, as well as the lake-effect band and vortices. In both the observations and simulation, the string of vortices developed along a cyclonic horizontal shear zone near the northern edge of the band and propagated toward the center of the band, in concert with the ascending branch of the transverse circulation. Soon after band formation, a connection was evident between the Lake Ontario band and another upstream LLAP band originating over Georgian Bay. As boundary layer winds backed from northwesterly to westerly over the upstream lakes, this connection was terminated and the string of vortices vanished.

These analyses further reveal that two separate criteria for the release of HSI, RIC and FIC, are satisfied along the shear zone and in the general location of the vortices, strongly suggesting that the release of HSI is the likely mechanism of misovortexgenesis in this case. Further-

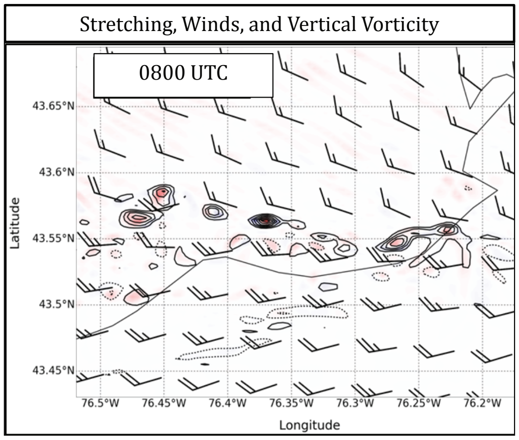

FIG. 11. Stretching term in the vertical vorticity equation ($\zeta \frac{\partial w}{\partial z} \times 10^{-4}$ s^{-2}; shaded), 500 m winds (full barb = 10 m s^{-1}), and vertical vorticity (contoured every 0.5 × 10^{-2} s^{-1}) at 0800 UTC.

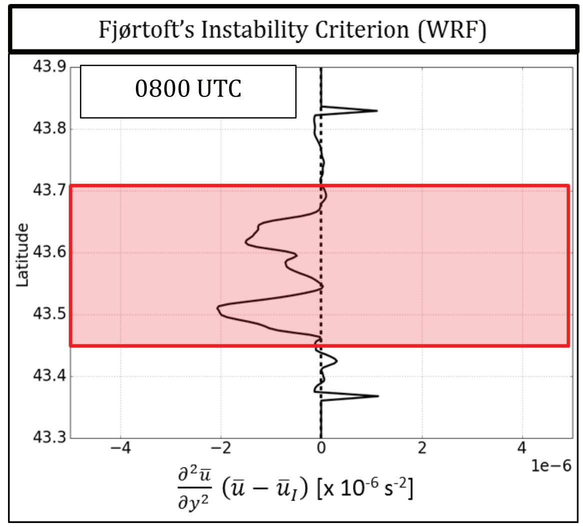

FIG. 13. FIC ($\frac{\partial^2 \bar{u}}{\partial y^2}(\bar{u} - \bar{u}_I) \times 10^{-6}$ s^{-2}) vs. latitude from the WRF simulation at 500 m AGL at 0800 UTC. The red shading indicates where FIC is satisfied.

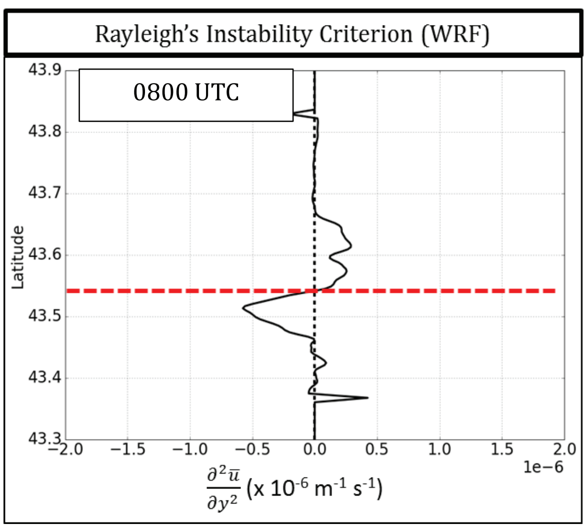

FIG. 12. RIC ($\frac{\partial^2 \bar{u}}{\partial y^2} \times 10^{-6}$ m^{-1} s^{-1}) vs. latitude from the WRF simulation at 500 m AGL at 0800 UTC. The red dashed line indicates where RIC is satisfied.

more, the lack of any notable anticyclonic misovortices or counter-rotating vortex couplets implies that tilting of ambient horizontal vorticity owing to the vertical wind shear by the updraft within the band is likely not the primary mechanism driving vortex formation. Analyses of the stretching term in the vertical vorticity equation reveal that stretching of vorticity by the band updraft helps maintain the vortices as they traverse the warm lake waters. After the vortices move inland, they quickly dissipate as the primary updraft weakens with the loss of lake-induced low-level destabilization and hence vortex stretching.

The results presented herein stem from a case study of only one intense LLAP band. Questions remain whether the release of HSI and subsequent stretching are the dominant formation mechanisms of misovortices in other LLAP bands. Furthermore, although the string of vortices vanishes in this case when the connection to the upstream band terminated, a preliminary analysis of other LLAP bands over Lake Ontario reveals that a connection to an upstream band is not necessary for such strings of vortices to exist. It is also unclear how the cyclonic shear zones within the bands along which the vortices form and propagate originate. Possible explanations for these phenomena include land-breeze circulations, either over Lake Ontario directly or possibly from an upstream lake, preexisting shear zones owing to upstream bands, preexisting mesoscale or synoptic scale wind shifts along which the bands can develop, or the transverse in-up-and-out circulation of the bands themselves. It is possible that the genesis of shear zones in different bands are attributable to different mechanisms, or that more than one of these processes is active simultaneously. For example, it is likely that the transverse circulation within the band sharpens the shear zone (hence increasing the near-surface vertical vorticity) via low-level convergence regardless of its origin. It is our hope that additional studies of other bands containing such strings of vortices will be attempted in the near future to investigate the causes of these shear zones, and whether some of the conclusions reached herein are applicable to other bands containing strings of vortices. For additional analysis of the present case, please see Mulholland et al. (2017).

Acknowledgments. The authors are grateful to the many participants (too numerous to mention) in the OWLeS Project who collected data in often formidable and adverse winter weather conditions. We also thank Rachel Humphries and Paul Robinson of the Center for Severe Weather Research (CSWR) who assisted with post-processing of the Doppler-on-Wheels (DOW) data; Professor Robert Ballentine (Retired; SUNY-Oswego), Tyler Kranz (University of Arizona), Dillon Ulrich (University of Utah), Dr. Brian Jewett, Andrew Janiszeski, and Chuan-Chieh Chang (University of Illinois at Urbana-Champaign; UIUC) for their assistance with the WRF model simulation; and Benjamin Vega-Westhoff, Chen Wang, Kenneth Patten, and David Wojtowicz (UIUC) for computing assistance. Financial support for this work from National Science Foundation Grant AGS 12-59257 is also acknowledged.

REFERENCES

Arnott, N., Y. Richardson, J. Wurman, and E. N. Rasmussen, 2006: Relationship between a weakening cold front, misocyclones, and cloud development on 10 June 2002 during IHOP. *Mon. Wea. Rev.*, **134**, 311-335.

Barnes, S. L., 1964: A technique for maximizing details in numerical weather map analysis. *J. Appl. Meteor.*, **3**, 396–409.

Bell, M. M., W. C. Lee, C. A. Wolff and H. Cai, 2013: A Solo-based automated quality control algorithm for airborne tail Doppler radar data. *J. Appl. Meteor. Climatol.*, **52**, 2509-2528.

Buban, M. S., C. L. Ziegler, E. N. Rasmussen, and Y. R. Richardson, 2007: The dryline on 22 May 2002 during IHOP: Ground-radar and in situ data analysis of the dryline and boundary layer evolution. *Mon. Wea. Rev.*, **135**, 2473-2505.

Campbell, P. C., B. Geerts, and P. T. Bergmaier, 2014: A dryline in southeast Wyoming. Part I: Multiscale analysis using observations and modeling on 22 June 2010. *Mon. Wea. Rev.*, **142**, 268-289.

Conrad, D. M., N. Zelasko, J. W. Frame, and J. Mulholland, 2015: Mobile Doppler radar observations of an intense long lake-axis parallel lake-effect snowband on 10-12 December 2013 during the Ontario Winter Lake-effect Systems Project. *19th Conf. on Air-Sea Interaction*, Phoenix, AZ, Amer. Meteor. Soc.

Iacono, M. J., J. S. Delamere, E. J. Mlawer, M. W. Shephard, S. A. Clough, and W. D. Collins, 2008: Radiative forcing by long-lived greenhouse gases: Calculations with the AER radiative transfer models. *J. Geophys. Res.*, **113**, D13103.

Jiménez, P. A., J. Dudhia, J. F. Gonza lez-Rouco, J. Navarro, J. P. Monta vez, and E. Garci a-Bustamante, 2012: A revised scheme for the WRF surface layer formulation. *Mon. Wea. Rev.*, **140**, 898-918.

Kosiba, K., J. Wurman, Y. Richardson, P. Markowski, P. Robinson, and J. Marquis, 2013: Genesis of the Goshen County, Wyoming, tornado on 5 June 2009 during VORTEX2. *Mon. Wea. Rev.*, **141**, 11571181.

Kristovich, D. A. R., and Coauthors, 2017: The Ontario Winter Lake-effect Systems (OWLeS) Field Project. *Bull. Amer. Meteor. Soc.*, **98**, 315-332.

Lee, B. D. and R. B. Wilhelmson, 1997: The numerical simulation of non-supercell tornadogenesis. Part I: Initiation and evolution of pretornadic misocyclone circulations along a dry outflow boundary. *J. Atmos. Sci.*, **54**, 32-60.

Majcen, M., P. Markowski, Y. Richardson, D. Dowell, and J. Wurman, 2008: Multipass objective analysis of Doppler radar data. *J. Atmos. Oceanic Technol.*, **25**, 1845-1858.

Markowski, P., and Y. Richardson, 2010: *Mesoscale Meteorology in Midlatitudes*. Wiley-Blackwell, 407 pp.

Marquis, J. N., Y. P. Richardson, and J. M. Wurman, 2007: Kinematic observations of misocyclones along boundaries during IHOP. *Mon. Wea. Rev.*, **135**, 1749-1768.

Mueller, C. K. and R. E. Carbone, 1987: Dynamics of a thunderstorm outflow. *J. Atmos. Sci.*, **44**, 1879-1898.

Mulholland, J. P., J. W. Frame, S. W. Nesbitt, S. M. Steiger, K. A. Kosiba, and J. M. Wurman, 2017: Observations of misovortices within a long-lake-axis-parallel lake-effect snow band during the OWLeS Project. *Mon. Wea. Rev.*, **145**, 3265-3291.

Pauley, P. M., and X. Wu, 1990: The theoretical, discrete, and actual response of the Barnes objective analysis scheme for one and two-dimensional fields. *Mon. Wea. Rev.*, **118**, 1145-1163.

Phillips, D. W., 1972: Modification of surface air over Lake Ontario in winter. *Mon. Wea. Rev.*, **100**, 662-670.

Shin, H.H., and S-Y. Hong: Representation of the subgrid-scale turbulent transport in convective boundary layers at gray-zone resolutions. *Mon. Wea. Rev.*, **143**, 250-271.

Skamarock, W. C., and Coauthors, 2008: *A Description of the Advanced Research WRF Version 3.* NCAR Technical Note NCAR/TN-475+STR, doi:10.5065/D68S4MVH.

Smirnova, T. G., and Coauthors, 2016: Modifications to the Rapid Update Cycle land surface model (RUC LSM) available in the Weather Research and Forecasting (WRF) model. *Mon. Wea. Rev.*, **144**, 1851-1865.

Steiger, S. M. and Coauthors, 2013: Circulations, bounded weak echo regions, and horizontal vortices observed within long-lake-axis-parallel lake-effect storms by the Doppler on Wheels. *Mon. Wea. Rev.*, **141**, 2821-2840.

Thompson, G., P. R. Field, R. M. Rasmussen, and W. D. Hall, 2008: Explicit forecasts of winter precipitation using an improved bulk microphysics scheme. Part II: Implementation of a new snow parameterization. *Mon. Wea. Rev.*, **136**, 5095-5115.

Wurman, J. M., J. M. Straka, E. N. Rasmussen, M. Randall, and A. Zahrai, 1997: Design and deployment of a portable, pencil-beam, pulsed, 3-cm Doppler radar. *J. Atmos. Oceanic Technol.*, **14**, 1502–1512.